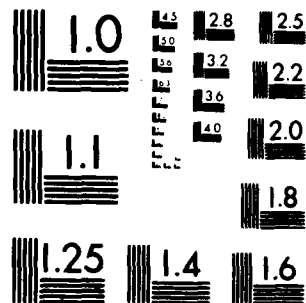


UNCLASSIFIED

CALIFORNIA UNIV SANTA BARBARA  
OPTICAL INVESTIGATIONS OF THE  
SEP 81 J L MERZ

COMBINATION PROCESSES IN LASER--ETC (U)  
F19628-79-C-0128  
RADC-TR-81-233

END  
DATE  
FILMED  
1 82  
PTIC



MICROCOPY RESOLUTION TEST CHART  
NATIONAL BUREAU OF STANDARDS 1963 A.

AD A108627

THIS REPORT WAS PREPARED BY THE BUREAU OF  
INVESTIGATION OF THE DEPARTMENT OF JUSTICE  
AT THE REQUEST OF THE ATTORNEY GENERAL

DATE: 10-15-43

APPROVED:

*Robert B. Darling*  
SPECIAL AGENT IN CHARGE  
BUREAU OF INVESTIGATION

APPROVED:

*James H. [Signature]*  
SPECIAL AGENT IN CHARGE  
BUREAU OF INVESTIGATION

FOR THE DIRECTOR:

*[Signature]*  
SPECIAL AGENT IN CHARGE  
BUREAU OF INVESTIGATION

IN WASH. D.C. OFFICE OF THE  
ATTORNEY GENERAL  
RECEIVED  
OCT 16 1943  
U.S. DEPT. OF JUSTICE

UNCLASSIFIED

SECURITY CLASSIFICATION OF THIS PAGE (When Data Entered)

REPORT DOCUMENTATION PAGE		READ INSTRUCTIONS BEFORE COMPLETING FORM
1. REPORT NUMBER RADC-TR-81-233	2. GOVT ACCESSION NO. AD-A108 627	3. RECIPIENT'S CATALOG NUMBER
4. TITLE (and Subtitle) OPTICAL INVESTIGATIONS OF THE RECOMBINATION PROCESSES IN LASER-ANNEALED AND THERMALLY- ANNEALED SEMICONDUCTORS		5. TYPE OF REPORT & PERIOD COVERED Interim Report 1 Jul 79 - 30 Jun 80
		6. PERFORMING ORG. REPORT NUMBER N/A
7. AUTHOR(s) James L. Merz		8. CONTRACT OR GRANT NUMBER(s) F19628-79-C-0128
9. PERFORMING ORGANIZATION NAME AND ADDRESS University of California Santa Barbara CA 93106		10. PROGRAM ELEMENT, PROJECT, TASK AREA & WORK UNIT NUMBERS 61102F 2306J234
11. CONTROLLING OFFICE NAME AND ADDRESS Deputy for Electronic Technology (ESO) Hanscom AFB MA 01731		12. REPORT DATE September 1981
		13. NUMBER OF PAGES 46
14. MONITORING AGENCY NAME & ADDRESS (if different from Controlling Office) Same		15. SECURITY CLASS. (of this report) UNCLASSIFIED
		15a. DECLASSIFICATION/DOWNGRADING SCHEDULE N/A
16. DISTRIBUTION STATEMENT (of this Report)  Approved for public release, distribution unlimited.		
17. DISTRIBUTION STATEMENT (of the abstract entered in Block 20, if different from Report)  Same		
18. SUPPLEMENTARY NOTES  RADC Project Engineer: Rudolph Bradbury (ESO)		
19. KEY WORDS (Continue on reverse side if necessary and identify by block number) Laser Annealing Electron Beam Annealing Indium Phosphide Silicon		
20. ABSTRACT (Continue on reverse side if necessary and identify by block number) Electron-beam-induced current and low temperature photoluminescence have been used as minority-carrier probes to investigate the perfection of beam-annealed silicon. Results for both laser and electron-beam annealing are reported. For CW laser annealing of ion implantation damage, the range of laser power over which good quality annealed material can be achieved is very limited, and strongly dependent on the substrate temperature during the anneal. At relatively high laser power, laser-induced		

DD FORM 1 JAN 73 1473

EDITION OF 1 NOV 65 IS OBSOLETE

UNCLASSIFIED

SECURITY CLASSIFICATION OF THIS PAGE (When Data Entered)

UNCLASSIFIED

SECURITY CLASSIFICATION OF THIS PAGE(When Data Entered)

damage is observed, and misfit dislocations are introduced for laser power just below that required to melt the substrate. Superior results are obtained with the use of a scanning electron beam for annealing: the range of beam power is broader, and the amount of beam overlap for subsequent scans required to achieve good annealing is less for the electron beam case compared to the case of laser annealing. Both photoluminescence results indicate that the laser-induced damage is produced deeper in the substrate than the implanted layers. Estimates of the lattice displacement resulting from strain after laser annealing are made from the details of the photoluminescence spectra; this lattice displacement is found to be small, corresponding to 0.01% of the lattice constant.

Accession For	
NTIS GPA&I	<input checked="checked" type="checkbox"/>
DTIC TAB	<input type="checkbox"/>
Unannounced	<input type="checkbox"/>
Justification	
By	
Distribution/	
Availability Codes	
Dist	Avail and/or Special
A	

UNCLASSIFIED

SECURITY CLASSIFICATION OF THIS PAGE(When Data Entered)

## I. INTRODUCTION

Interest in the use of ion implantation for the fabrication of semiconductor devices has increased with the recent reports by Russian<sup>(1)</sup> and Italian<sup>(2)</sup> research groups that the damage produced in the lattice during implantation can be annealed with intense pulses of laser radiation. This so-called "laser annealing" of the lattice damage offers a high degree of lateral control over the annealed region of the device. Moreover, the annealing takes place on a time scale considerably shorter than that associated with conventional thermal annealing processes, reducing the possibility of sample contamination or even decomposition. In this "giant-pulse" regime of laser annealing, the sample melts and recrystallizes in times of the order of several 100 nsec. More recently another regime of laser annealing has been explored,<sup>(3,4)</sup> in which a scanned CW ion laser is used to produce a solid-phase epitaxial regrowth of the implanted layer in times of the order of msec. Both the pulsed and CW annealing regimes can also be effected by the use of electron beams instead of laser beams. A number of encouraging results have already been reported for the laser annealing of implanted Si: the residual damage, as measured by Rutherford backscattering, is low after laser annealing, the percent of substitutional dopant impurities is high, and the resulting electrical activity of annealed layers is good.

In particular, it has been reported that CW laser annealing of implanted Si with a scanned Ar<sup>+</sup> ion laser produces good-quality, defect-free single-crystal material over a reasonable range of laser power (approximately 80-95% of the laser power necessary to melt the Si crystal).<sup>(3-5)</sup> In some instances the solid solubility of the implanted

species has been exceeded by laser annealing compared with thermal treatments.<sup>(6)</sup> More recently, however, DLTS<sup>(7)</sup> and photoluminescence<sup>(8,9)</sup> studies have shown that electrically and optically active defects are present in the laser-annealed material. Defects can dominate the minority carrier lifetime, one of the most important indications of material quality for actual device performance. Therefore, beam annealing (using both lasers and electron beams) requires additional characterization using techniques which reflect minority-carrier effects rather than majority-carrier properties.

The aim of the research program described in this report is to conduct an investigation of minority carrier recombination processes in ion-implanted semiconductors which have been laser annealed by using optical techniques; in particular, the low temperature photoluminescence of excitons bound to implanted donors and acceptors is investigated. In addition, consistent with the approach of studying minority-carrier effects in beam-annealed semiconductors, the scope of this investigation has been broadened in two ways.

1. Electron-beam-induced-current (EBIC) measurements have been used to complement the photoluminescence studies as another powerful technique to determine minority-carrier properties. EBIC provides information about minority carrier recombination in these materials, since regions of high defect density or amorphous material will appear as dark areas in the EBIC display.<sup>(10)</sup>

2. The beam annealing studies have been extended to the use of scanned-electron-beam annealing (SEBA) in addition to the CW laser annealing (LA) originally envisioned for these studies. Some preliminary experiments on using giant-pulse laser annealing have also been initiated, but these results will be reported elsewhere.



Thus far, the results of these investigations have been obtained on Silicon, and may be summarized briefly as follows.

A. Summary of Laser-Annealing Results

1. Both photoluminescence and EBIC experiments show that the "window" for successful laser annealing is quite small; low charge-collection efficiency, with a high-contrast pattern of light and dark stripes running parallel to the laser scan, usually results.

2. This window is a function of the substrate temperature during the anneal.

3. Optimum annealing is obtained for a highly-overlapping scan of a large-diameter (approximately 100  $\mu\text{m}$ ) laser spot, at a laser power just above the threshold for the initiation of annealing (approximately 70-75% of the power required for melting).

4. At lower laser power, inadequate annealing results in low charge collection efficiency.

5. At higher laser power, there is strong evidence for the existence of laser-induced damage, which extends into the bulk of the wafer below the implanted layers. As the laser power approaches that required to melt the Si wafer, the damage takes the form of misfit dislocations.

6. From the observed broadening and shifting of bound-exciton luminescence lines after laser annealing, the strain surrounding the implanted ions was found to be quite small, corresponding to approximately  $10^{-4}$  of the original lattice displacement.

## B. Summary of Electron-Beam-Annealing Results

1. Electron-beam annealing is found to be generally superior to laser annealing in most respects thus-far investigated. Dark stripes are difficult to observe in the EBIC display, and the charge collector current is greater.

2. The window for successful electron-beam annealing is broader and flatter than that for laser annealing.

3. The required beam overlap is considerably less than that required for good laser annealing.

4. Only when the electron-beam power approaches that required for melting does the charge collection efficiency fall off; it does so rapidly as a result of the formation of misfit dislocations.

## II. EXPERIMENTAL TECHNIQUES

### A. Laser-Annealing Apparatus

An 18 Watt  $\text{Ar}^+$  ion laser with multi-line output was used for most of the laser annealing experiments, although a few experiments were performed initially with a  $\text{Kr}^+$  ion laser utilizing approximately 6 Watts. The scanning system is shown in Fig. 1. A galvanometer-driven mirror is used for the y-direction scan, and the sample holder is mounted on a translation stage for the x-scan. The y-scan speed can be varied between 0.1 and 20 cm/sec., and at the end of each y-scan, the stage is shifted by a stepping motor with minimum steps of 6  $\mu\text{m}$ . During the annealing, the sample is mounted on a vacuum chuck, and heated to the desired temperature. The beam diameter ( $1/e$  width of the Gaussian beam) is determined by the focal length and distance of the lens used to focus the light on the sample. Typical annealing conditions are given in Table I.

(7)

TABLE I  
BEAM ANNEALING PARAMETERS

	LASER	ELECTRON-BEAM
	Spectra Physics Argon laser Model 171-19	JEOL Scanning Electron Microscope modified for high current operation
Substrate temperature	250°C	20°C
Beam power	10-15 W	150 $\mu$ a at 30 kV
Working distance	--	26 mm
Beam size	100 $\mu$ m	20 $\mu$ m
X-step	6 $\mu$ m	11 $\mu$ m
Y-scan	6 cm/sec	20 cm/sec

### B. Electron-Beam-Annealing Apparatus

For scanned-electron-beam annealing, a commercial Etek scanning electron microscope was modified for high current operation; this is done by removing appropriate apertures from the gun assembly to obtain sufficiently high beam currents for annealing. Beam currents as high as 150  $\mu\text{A}$  were achievable. All anneals were done at room temperature. Typical conditions for anneals are also given in Table I.

### C. Sample Preparation

Samples were implanted with energies between 25 and 180 keV and typical doses of  $5 \times 10^{14}$ - $2 \times 10^{16}$   $\text{As}^+$  ions/ $\text{cm}^2$  into p-type Si substrates whose resistivity ranged from 5 to 20 ohm cm. To compare our results with those obtained in other laboratories, a few samples were obtained from other sources. One set of samples was implanted and  $\text{Ar}^+$  laser annealed at Stanford University using the two-mirror scanning system previously described.<sup>(11)</sup> A second group was implanted at Xerox Corporation, El Segundo, and  $\text{Kr}^+$  or  $\text{Ar}^+$  laser-annealed at the University of California, Santa Barbara (UCSB). However, unless otherwise indicated, all data reported here were obtained on samples both implanted and laser-annealed at UCSB. For photoluminescence experiments, samples were implanted with lower doses of  $\text{P}^{++}$  as explained in Section III, C.

### D. EBIC Measurements

After implantation and beam annealing, mesa diodes were fabricated by standard photolithographic techniques and metallized ohmic contacts were formed on both sides of the sample. The area of the top ohmic contact is smaller than the mesa area in order that electrons can penetrate directly into the sample for EBIC measurements.

The principle of EBIC is shown in Fig. 2. The top of the sample is implanted (usually with  $\text{As}^+$ ) and annealed to become n-type, producing a p-n junction in the p-type (B-doped) substrate. The shaded area represents the depletion region. The electron beam from the SEM produces minority carriers, which diffuse and drift across the junction. This charge collection results in a current, which can be displayed on the cathode ray tube (CRT). Since a minority carrier will recombine at defect centers or improperly-annealed damage portion before reaching the depletion layer, such regions appear as dark areas due to a reduction in the charge collection efficiency. Thus, the CRT display provides a 2-D map of the regions of high and low charge collection efficiency, corresponding to low and high defect density, respectively. Moreover, depth information can also be obtained, since the penetration of primary electrons can be varied by changing the accelerating voltage. For example, the junction plane formed by a 100 keV As implant is approximately 0.2 to 0.3  $\mu\text{m}$  from the surface, whereas the range of the electron beam is 0.3  $\mu\text{m}$  for 5 keV, and 3  $\mu\text{m}$  for 20 keV.<sup>(12)</sup> Therefore, EBIC pictures taken with 5 keV accelerating voltage contain information mainly from the originally amorphous layer which is created by ion implantation, while the 20 keV pictures provide some substrate information. These effects are shown schematically in Fig. 2. Such arguments are, of course, qualitative; clearly there is some ambiguity due to the profile of the electron beam in the sample, carrier diffusion, and other effects. Quantitative estimates are complex, but can be carried out.<sup>(12)</sup>

To compare similar samples which have been annealed with different laser power, EBIC displays were obtained with identical electron beam current and amplifier gain. The total EBIC charge collection current,

$I_{\text{EBIC}}$  was measured for each sample, and is used as a measure of the charge collection efficiency of the laser-annealed sample. In addition, each sample was used as a simple photodetector, and the resulting short-circuit photocurrent,  $I_{\text{photo}}$ , as well as  $I_{\text{EBIC}}$  was used as a measure of the minority-carrier collection efficiency.

#### E. Photoluminescence Measurements

Low temperature photoluminescence measurements were carried out with the samples mounted in a liquid He immersion dewar. Temperatures between 4.2 and 1.6 K could be achieved by pumping the He below the lambda point. Luminescence was excited by low power output (typically < 100 mW) from the same  $\text{Ar}^+$  ion laser used for annealing experiments. The excitation wavelength was  $5145 \text{ \AA}$ , corresponding to a  $1/e$  penetration of the exciting light of approximately 2-3  $\mu\text{m}$ . A 1-meter McPherson monochromator with a dispersion of  $16 \text{ \AA/mm}$ , and an S-1 response photomultiplier cooled to  $-100^\circ\text{C}$ , with either phase-sensitive or photon-counting techniques, were used to detect the luminescence. The resulting resolution was sufficient to detect individual bound-exciton lines and determine broadening and shifts of these lines induced by stress. Spectral resolution is included with the data as appropriate.

#### F. Other Measurements

Sheet resistivity and Hall mobility measurements were frequently made on these samples after laser annealing, using the van der Pauw technique. It was also found useful to determine the return of amorphous implanted samples to their single-crystal condition after annealing by optical techniques, using either (1) an optical microscope to

observe differences in reflectivity, or, more precisely (2) an ellipsometer to compare the refractive index and absorption of unannealed and annealed layers with those of virgin Si.<sup>(13)</sup>

### III. RESULTS

#### A. EBIC Evaluation of Laser-Annealed Si

A typical EBIC result is shown in Fig. 3. In the upper and lower portions of this figure, the EBIC mode has been switched off so that a standard secondary-electron micrograph results. The laser-annealed sample appears to be smooth and defect-free in this mode, as anticipated. However, using the EBIC mode (center of Fig. 3), it is clear that laser annealing has produced quite non-uniform minority carrier effects: high-contrast dark lines appear which are parallel to the direction of laser scan. The EBIC dark-line spacing is of the order of the laser scan step; the deviations from constant spacing are believed to result from complex overlap effects, or small galvanometer deviations during scanning.

The sample shown in Fig. 3 is one of a series of "standard" samples processed at Stanford under conditions known to result in good-quality, defect-free single-crystal material.<sup>(3)</sup> It is clear, however, that laser annealing has produced quite nonuniform minority-carrier effects. Almost all samples studied here show such dark-line contrast. This dark-line contrast can result from two causes: (i) incomplete anneal due to insufficient laser power, allowing either a high density of residual defects or incomplete electrical activation of As donors; or (ii) damage induced by excess laser power, introducing crystal defects which act as recombination centers. Improved results were obtained for

a large-diameter laser beam (100  $\mu\text{m}$ ), small direction scan step (6  $\mu\text{m}$ ), and slow scan speed (6 cm/ sec). These results are consistent with recent photoluminescence data.<sup>(9)</sup>

An example of the results obtained with these parameters is shown in Fig. 4. The left column (Figs. 4(a)-(c)) shows the EBIC contrast pattern using 5 keV electrons; the right column (Figs. 4(d)-(f)) shows patterns obtained on the same 3 samples using 20 keV accelerating voltage. Consider first the 5 keV results;  $P$  is the laser power of the annealing beam. For  $P \leq 0.6P_M$ , where  $P_M$  is the power required for melting,<sup>(14)</sup> little EBIC contrast is observed, but the value of  $I_{\text{EBIC}}$  is very low. This value of  $P$  is clearly below the threshold for laser annealing. At  $P = 0.64P_M$ ,  $I_{\text{EBIC}}$  and  $I_{\text{photo}}$  increase, no sign of the implanted amorphous layer is observed optically, but strong contrast appears in the EBIC pattern, as seen in Fig. 4(a). At  $P = 0.72P_M$ ,  $I_{\text{EBIC}}$  and  $I_{\text{photo}}$  reach their maximum values, and the dark lines are much more difficult to see in the EBIC pattern (Fig. 4(b)). Increased laser power,  $P = 0.92P_M$ , produces a dramatic decrease in  $I_{\text{EBIC}}$  and  $I_{\text{photo}}$ , and a corresponding increase in EBIC contrast (Fig. 4(c)). Somewhat different results are obtained for 20 keV electrons.  $I_{\text{EBIC}}$  still peaks at approximately the same value of  $P$ , but strong contrast is observed only for large values of  $P$  (Fig. 4(f)), corresponding to laser power greater than that required for optimum anneal. In this case, a cross-hatched appearance is observed, resulting from the formation of misfit dislocations due to the thermal gradient-induced stress at this high laser power.

These results are typical; very similar effects were observed in many sets of samples prepared for these studies. Results for a lower



dose case are given in Fig. 5, which shows the dependence of  $I_{\text{photo}}$  and the sheet resistivity,  $\rho$ , on laser power. For this dose  $\rho = 45 \Omega/\square$  was achieved, corresponding to 100% electrical activation, and  $\mu_e = 40 \text{ cm}^2/\text{V sec}$ .  $I_{\text{photo}}$  peaks at a slightly higher value:  $P = 0.76P_M$ . As before,  $I_{\text{photo}}$  decreases at both low and high values of  $P$ . Also shown for comparison are the results for an electron-beam annealed (SEBA) and thermally annealed (TA) sample.

These results are interpreted as follows. The true "window" for optimum laser annealing, as determined by minority-carrier charge collection, is quite narrow, corresponding to  $\sim 70\text{-}75\%$  of  $P_M$ . The position of this window is weakly dose-dependent. At lower  $P$ , the anneal is incomplete. At values of  $P$  above the peak, the charge-collection efficiency drops off rapidly. This is direct evidence of laser-induced damage, and this damage is clearly observed at high accelerating voltage. Although it is difficult to extract accurate quantitative information from such experiments, these results strongly suggest that the laser-induced damage may extend considerably deeper than the implanted amorphous layer. This is consistent with the profile of non-radiative defect centers measured by DLTS.<sup>(7)</sup> For the case shown in Fig. 4(f), the observed misfit dislocations run from the surface deep into the crystal.

The data shown in Fig. 5 determines the "window" for optimum laser annealing as seen by these minority carrier measurements. The dependence of this window on processing parameters is of considerable interest for device application. In Fig. 6 the effect on this window of changing the substrate temperature during laser anneal is shown. A somewhat arbitrary definition of the annealing window has been used as

follows: The threshold power for good anneal corresponds to 100% activation, given by the point at which the sheet resistivity reaches a minimum value (e.g.,  $P = 0.69 P_M$  in Fig. 5). The upper-limit for good annealing is defined as the power at which  $I_{photo}$  is 10% of its maximum value. The melting power itself is dependent on substrate temperature (also shown in Fig. 6), as expected from calculation. Although no noticeable change in window width is observed over a wide range of temperature, it is noted that the position of the window with respect to the melting power is clearly dependent on substrate temperature. This is of particular importance for the practical application of processing of Si.

#### B. EBIC Evaluation of Electron-Beam Annealed Si

In general, the use of the scanned electron beam from the electron microscope gives results that are somewhat similar but generally superior to those obtained with the scanned laser beam (see, for example, Fig. 5). A direct comparison between the two techniques is given in Fig. 7, showing samples that have been optimally annealed using the two techniques. For the laser-annealed sample, Fig. 7(a), dark-line contrast, though weak, is still observable, while contrast in the electron-beam annealed sample is much weaker. Correspondingly, the optimum value of  $I_{photo}$  is slightly higher for electron-beam than for laser annealing. This implies that the electron-beam annealed sample has a uniformly high minority carrier collection efficiency.

In Fig. 7, the laser annealing was done with a high degree of overlap of each consecutive scan (i.e., more than 90% overlap). On the other hand, the degree of overlap required for uniform annealing is

the electron beam is much less. This is shown in Fig. 8. In the lower photograph, the x-step between successive scans is  $44\text{ }\mu\text{m}$ , while for Fig. 8(b) the step is  $22\text{ }\mu\text{m}$ , and in the top, Fig. 8(a), a step of  $11\text{ }\mu\text{m}$  results in very uniform annealing. The beam diameter was estimated to be  $\sim 20\text{ }\mu\text{m}$  by scanning it across a Faraday cup, although there is some ambiguity in determining this diameter, particularly because the electron beam spreads as it penetrates the sample (beam-blooming). Nevertheless, this figure shows that less overlap is required for electron-beam compared to laser annealing.

Furthermore, the window for electron-beam annealing is wider and flatter than that observed for laser annealing, as shown in Fig. 9. The plot of  $I_{\text{photo}}$  versus laser power for the laser-annealed (LA) sample at  $350^{\circ}\text{C}$  is identical to that shown in Fig. 5. However, for comparison with the electron-beam annealing (SEBA) done at room temperature, the LA curve obtained with a substrate temperature of  $25^{\circ}\text{C}$ , also shown, is more appropriate. Two major differences are immediately apparent. First, the electron-beam annealing produces a wide, flat window, compared to the laser-anneal curve, which peaks sharply at a power determined by the substrate temperature. Secondly, when the electron beam curve falls off, it does so precipitously; that is, the sample goes from good quality material to a state of high misfit dislocation or slip-plane density for a very small increase in beam power. It is difficult to observe an intermediate region, where damage is introduced by the laser without the formation of dislocations, in the case of the electron beam. These misfit dislocation networks are shown in Fig. 10. Networks are formed for both the laser and SEBA cases, with only slightly different appearance; these differences may be due to the different power level involved in annealing.

### C. Photoluminescence Evaluation of Laser-Annealed Si

Low temperature, bound-exciton luminescence of donors and acceptors in Si has been studied in detail.<sup>(15-23)</sup> However, there are two additional complications involved in the investigation of laser-annealed ion-implanted materials: (1) the luminescence intensities are generally quite weak, due to the presence of unannealed strain and damage in the vicinity of the implanted ion, and (2) the penetration of the implanted ions is quite low, typically only a few tenths of a  $\mu\text{m}$ , so that efficient overlap of the impurity distribution and the exciting light is difficult. The first of these difficulties is, of course, the point of using low temperature luminescence to investigate the quality of beam-annealed material; this technique has earlier been used by the principal investigator<sup>(24-30)</sup> and others<sup>(31)</sup> to evaluate the thermal anneal of implanted materials. As for the second difficulty, a multiple-energy implantation of  $\text{P}^{++}$  was performed with a maximum energy of 180 keV to create a deep and uniform P concentration profile, so that enhanced luminescence intensity could be obtained. Typically, a flat profile of P with a concentration of  $10^{16} \text{ cm}^{-3}$  to a depth of  $\sim 0.6 \mu\text{m}$  was used. This concentration was chosen to prevent concentration quenching of the luminescence.<sup>(20)</sup> Since the penetration of the  $\text{Ar}^+$  laser excitation into the sample was  $\sim 2-3 \mu\text{m}$ , which is deeper than the implanted layer thickness of  $\sim 0.6 \mu\text{m}$ , some of the luminescence observed was from the B doping of the p-type substrate. This luminescence was used to evaluate any deterioration or creation of damage in the substrate as a result of the implant or the beam processing. P-related luminescence is expected only from the implanted layer, since there was no additional P doping other than the implant.

A typical luminescence spectrum obtained for a P-implanted and thermally-annealed sample is shown in Fig. 11. The higher energy region of the spectrum shows the recombination of excitons bound to neutral B and P; these are no-phonon lines, and are designated  $B_{NP}$  and  $P_{NP}$ .<sup>(16)</sup> Additional weak lines, denoted  $B_{NP}(b_i)$ , etc., result from bound multi-exciton complexes.<sup>(22,23)</sup> In the lower energy region, the emission lines consist of momentum-conserving phonon replicas of the no-phonon lines; these are denoted by  $B_{LO}$ ,  $B_{TO}$ , etc., to indicate the type of phonon involved. Note that in this and the following figures, the intensities of the no-phonon lines and the TO phonon lines are independently normalized for clarity of presentation.

Very similar spectra were obtained from laser-annealed samples with annealing laser power ranging from 0.6 to 0.95 of the melting power ( $P_M$ ) for Si. Figure 12 shows the results for P: the luminescence intensity for the  $P_{NP}$  emission line is plotted as a function of the annealing power, relative to the melting power,  $P_M$ . No luminescence signal is observed below  $0.6 P_M$ , indicating that this laser power was insufficient for activation of the implanted P. However, a sharp increase is observed between  $0.6$  and  $0.7 P_M$ , which clearly shows activation of the implanted species. This result is fully consistent with the electrical activation results obtained by sheet resistivity measurements (cf. Fig. 5), for which  $4 \times 10^{15}$   $As^+$  ions/cm<sup>2</sup> were implanted into the same substrate material and laser annealed. The luminescence results, on the other hand, were obtained for low-dose  $P^{++}$  implants, below the dose necessary to make the Si amorphous. The similarity of these results suggests that the implant dose does not have a strong influence on the laser power required for the activation of implanted impurities. After

reaching a maximum intensity, the luminescence decreases with increasing laser power, despite the fact that there is no change in the degree of electrical activation (as shown by the sheet resistivity data of Fig. 5). This decrease in intensity must therefore be due to the reduction of the minority carrier lifetime and/or creation of non-radiative defects. An alternate explanation, involving small displacements of the P atom from its substitutional lattice site (for which electrical measurements are far less sensitive than optical measurements) is considered unlikely on the basis of the very small lattice displacements estimated from the optical data to be described below.

For the case of B luminescence, a similar dependence on laser power was observed, as shown in Fig. 13. However, the reason for this power dependence must be somewhat different than for the P case, since this luminescence originates from B acceptors in the original substrate material. The exciting light penetrates deeper than the implanted layer, exciting luminescence from the substrate B. Thus, even for laser power less than  $0.6 P_M$  (for which no P luminescence was observed), the B luminescence intensity was already ~30-40% of its maximum value. For increasing laser power, the B luminescence intensity also increases, as a result of at least two effects: (1) B in the implanted layers also becomes optically active as a result of the laser annealing, and (2) the absorption coefficient of the implanted layer is reduced, so that more substrate B can be excited. Finally, the reduction in luminescence intensity above  $0.75 P_M$  can be attributed to the production of defects at high laser power, as was the case for the P-luminescence. However, there is again the difference that most of the optically-active B is expected to be in the substrate below the implanted layer, so that

that the laser-induced defects also extend quite deep into the substrate. This is consistent with the short-circuit photocurrent,  $I_{\text{photo}}$ , obtained for a higher dose implant, and also plotted in Fig. 13.

The strain which exists after laser annealing can also be estimated from the detailed line-shape of the no-phonon lines. For this purpose, a high resolution spectrum in the region of the no-phonon lines is shown in Fig. 14. For a sample doped with P during growth, the half-width measured for the  $P_{\text{NP}}$  lines is very small, and is instrument-limited in Fig. 14. However, for  $P$ -implanted samples, both a conventional thermal anneal (TA) and a laser anneal show increased half-widths, indicating that the implant damage has not been completely removed. As the laser power increases, the linewidth also increases until, at  $\sim 0.94 P_M$ , the peak of the line begins to shift to lower energy. This laser power is sufficient to induce damage; consequently a strain field exists at the impurity. By comparing this data with published uniaxial stress data for P-doped Si, <sup>(21,22)</sup> an estimate can be made of the strain-induced lattice displacement,  $\Delta a/a$ . The maximum displacement observed in these experiments, at a laser power corresponding to  $0.94 P_M$ , was only  $\Delta a/a = 10^{-4}$ , a surprisingly small amount. For this value of laser power, misfit dislocations form, as was seen in Figs. 4 and 10. Thus, the strain field is relaxed by the introduction of these dislocations. At lower laser power, where no misfit dislocations are observed, the lattice displacement is clearly seen to be very small.

#### IV. CONCLUSIONS AND FUTURE PLANS

Considerable information about the mechanisms of beam annealing implanted Si has been gained by the study of minority carrier effects

using electron-beam-induced current and low temperature photoluminescence. The detailed results of this investigation have been summarized in the Introduction. It is clear that good-quality material suitable for device application can be obtained by laser annealing, requiring considerable care, since the window for annealing is much narrower than had been indicated in the literature, and damage can easily be introduced by the laser. However, using scanned electron-beam annealing the control tolerances to achieve good results are somewhat relaxed, and the quality of the resulting material is generally superior.

During the second year of this investigation, two major areas need to be investigated. For Si, the nature of the laser-induced damage needs to be further explored, and the use of these beam annealing techniques for actual devices should be investigated. Secondly, much of this work will be extended to InP and related compound semiconductors. Work on the compound semiconductors is currently receiving a high priority in this laboratory.

#### V. PERSONNEL

The following people have been actively engaged in these investigations:

Dr. James L. Merz, Professor, Department of Electrical and Computer Engineering, UCSB.

Dr. Masashi Mizuta, Postdoctoral Research Fellow, Tokyo Institute of Technology.

Mr. Neng-Haung Sheng, Graduate Student, Department of Electrical and Computer Engineering, UCSB.



In addition, the contributions of the following are gratefully acknowledged:

Professor James F. Gibbons and Drs. A. Lietoila and R.B. Gold, Stanford University, for collaborative assistance during the early phases of this work. Professor H. Kroemer, UCSB, and Drs. C.L. Anderson and L.C. Hess, Hughes Research Laboratory, for technical discussions. Dr. Zuo-Liang Wu, People's Republic of China, and Mr. Don Zak, UCSB, for technical assistance. Dr. Michael Lo, Xerox Laboratory, for implanted samples.

#### VI. PUBLICATIONS AND CONFERENCE TALKS

The following papers and abstracts are attached to this report:

1. "Electron-Beam-Induced Current Investigations of CW Laser-Annealed Silicon," by Mizuta, Sheng, Merz, Lietoila, Gold, and Gibbons, Applied Physics Letters, 37, 154 (15 July 1980).
2. "EBIC and Luminescence Investigations of CW Laser-Annealed and Electron-Beam Annealed Silicon," by Mizuta, Sheng, and Merz, paper presented at the Electronic Materials Conference, Cornell University, June 23-27, 1980.
3. "EBIC Investigation of Defects in Beam-Annealed Si," by Sheng, Mizuta, and Merz, abstract submitted and accepted for presentation at the Materials Research Society Annual Meeting in Boston, Mass., Nov. 16-21, 1980.

## REFERENCES

1. E.I. Shtyrkov et al., Sov. Phys. Semicond. 9, 1309 (1976); A.Kh. Antonenko et al., ibid 10, 81 (1976); O.G. Kozlov et al., ibid 10, 265 (1976).
2. H.D. Geiler et al., Phys. Stat. Sol. (a) 41, K171 (1977); G. Foti et al., Appl. Phys. 14, 189 (1977); J. Krynichi et al., Phys. Lett. A61, 181 (1977).
3. A. Gat, J.F. Gibbons, V.R. Deline, P. Williams, and C.A. Evans, Jr., Appl. Phys. Lett. 32, 276 (1978).
4. L.D. Hess, R.A. Forber, S.A. Kokorowski, and G.L. Olson, Proc. Soc. Photo-Opt. Instr. Engineers 198, 31 (1979).
5. D.H. Auston, J.A. Golovchenko, P.R. Smith, C.M. Surko, and T.N.C. Venkatesan, Appl. Phys. Lett. 33, 539 (1978).
6. A. Lietoila, J.F. Gibbons, T.J. Magee, J. Peng and J.D. Hong, Appl. Phys. Lett. 35, 532 (1979).
7. N.M. Johnson, R.B. Gold, and J.F. Gibbons, Appl. Phys. Lett. 34, 704 (1979).
8. R.A. Street, N.M. Johnson, and J.F. Gibbons, J. Appl. Phys. 50, 8201 (1979).
9. R.A. Street and N.M. Johnson, Laser and Electron Beam Processing of Materials, edited by C.W. White and P.S. Peercy (Academic Press, N.Y., 1980), p. 435.
10. L.C. Kimerling, H.J. Leamy, J.L. Benton, S.D. Ferris, P.E. Freeland, and J.J. Rubin, Semicond. Silicon/1977 (Electronics Research Laboratory, Princeton, 1977), p. 468.

11. A. Gat and J.F. Gibbons, Appl. Phys. Lett. 32, 142 (1978).
12. T.E. Everhart and P.H. Hoff, J. Appl. Phys. 42, 5837 (1971).
13. K. Watanabe, M. Miyao, I. Takemoto, and N. Hashimoto, Appl. Phys. Lett. 34, 518 (1979).
14. Melting is determined by optical microscope observation for 50  $\mu$ m steps.
15. J.R. Haynes, Phys. Rev. Letters 4, 361 (1960).
16. P.J. Dean, J.R. Haynes, and W. Flood, Phys. Rev. 161, 711 (1967);  
ibid 163, 721 (1967).
17. R.B. Hammond, T.C. McGill, and J.W. Mayer, Phys. Rev. B13, 3566 (1976).
18. K.R. Elliot et al., Phys. Rev. B17, 1808 (1978); S.A. Lyon et al.,  
ibid B17, 2620 (1978).
19. T.C. McGill, Solid State Electr. 21, 1339 (1978).
20. M. Tajima, Appl. Phys. Lett. 32, 719 (1978).
21. R. Sauer and J. Weber, Phys. Rev. Lett. 36, 48 (1976).
22. M.L.W. Thewalt and J.A. Rostworowski, Phys. Rev. Lett. 41, 808 (1978).
23. G. Kirczenow, Can. J. Phys. 55, 1788 (1977).
24. J.L. Merz and L.C. Feldman, Appl. Phys. Lett. 15, 129 (1969).
25. J.L. Merz, L.C. Feldman, and E.A. Sadowski, Rad. Effects 6, 285 (1970); Ion Implantation, edited by F.H. Eisen and L.T. Chadderton (Gordon and Breach, London, 1971), p. 269.
26. L.C. Feldman, W.M. Augustyniak and J.L. Merz, Rad. Effects 6, 293 (1970); Ion Implantation, edited by F.H. Eisen and L.T. Chadderton (Gordon and Breach, London, 1971), p. 277.

27. J.L. Merz, Proceedings of 10th International Conf. on the Physics of Semiconductors, edited by S.P. Keller, J.C. Hensel, and F. Stern (U.S. Atomic Energy Commission, Oak Ridge, 1970), p. 251.
28. J.L. Merz, J. Appl. Phys. 42, 2463 (1971).
29. J.L. Merz, E.A. Sadowski, and J.W. Rodgers, Solid State Commun. 9, 1037 (1971).
30. J.L. Merz, L.C. Feldman, D.W. Mingay, and W.M. Augustyniak, Proceedings of II International Conf. on Ion Implantation in Semiconductors, Bavaria, Germany, edited by I. Ruge and J. Graul (Springer-Verlag, NY, 1971), p. 182.
31. D.J. Welford et al., J. Appl. Phys. 48, 2442 and 2453 (1977); Appl. Phys. Lett. 28, 711 (1976).

## FIGURE CAPTIONS

- Fig. 1. Schematic diagram and typical conditions used for laser and scanning electron beam annealing.
- Fig. 2. Schematic diagram of the electron-beam-induced current experiments.
- Fig. 3. EBIC micrograph (center) and secondary electron emission image (top and bottom) excited by 5-keV beam. The sample was implanted with  $6 \times 10^{14}$   $\text{As}^+$  ions/ $\text{cm}^2$  and annealed with a 40- $\mu\text{m}$  spot and 30- $\mu\text{m}$  step. In the EBIC mode, dark regions correspond to low charge collection. Substrate temperature  $T_S = 250^\circ\text{C}$ .
- Fig. 4. EBIC micrographs for  $1.6 \times 10^{16}$   $\text{As}^+$  ions/ $\text{cm}^2$  annealed with a 100- $\mu\text{m}$  spot and 6- $\mu\text{m}$  step. Left column (a)-(c) for 5 and right (d)-(f) for 20 keV. Annealing laser power was 0.64  $P_M$  for (a) and (d), 0.72  $P_M$  for (b) and (e), and 0.92  $P_M$  for (c) and (f).  $T_S = 250^\circ\text{C}$ .
- Fig. 5. Dependence of short-circuit current  $I_{\text{photo}}$  in arbitrary units and sheet resistivity  $\rho$  on annealing laser power  $P$  for  $4 \times 10^{15}$   $\text{As}^+$  ions/ $\text{cm}^2$  sample with 100- $\mu\text{m}$  laser spot and 6- $\mu\text{m}$  step. Laser power is normalized by the melting power  $P_M$ .  $T_S = 250^\circ\text{C}$ . Also shown are electron-beam annealed (SEBA) and thermally annealed (TA) samples.
- Fig. 6. Dependence of the laser power required for melting ( $P_M$ ), and the window for good annealing, on substrate temperature. Triangles give the threshold (i.e., lowest) power for good annealing, closed circles represent the upper-limit power for annealing as described in the text.

Fig. 7. EBIC micrographs for (a) laser anneal and (b) electron-beam annealing under optimal anneal conditions for each technique.

Fig. 8. EBIC micrographs for electron-beam annealing showing the effect of beam overlap. Scan speed: (a) 44  $\mu\text{m}$ . Diameter of electron beam is  $\sim 20 \mu\text{m}$ .

Fig. 9. Dependence of short-circuit current,  $I_{\text{photo}}$ , in relative units, on annealing laser power for samples laser-annealed (LA) at two different substrate temperatures and a sample electron-beam annealed (SEBA) at room temperature. Laser power is normalized by the melting power,  $P_M$ .

Fig. 10. EBIC micrographs showing the introduction of misfit dislocations for (a) laser annealing and (b) electron-beam annealing.

Fig. 11. Low temperature photoluminescence spectrum for  $P^{++}$  implanted into B-doped Si, followed by conventional thermal anneal. The implant conditions and the resulting spectral features are explained in the text.

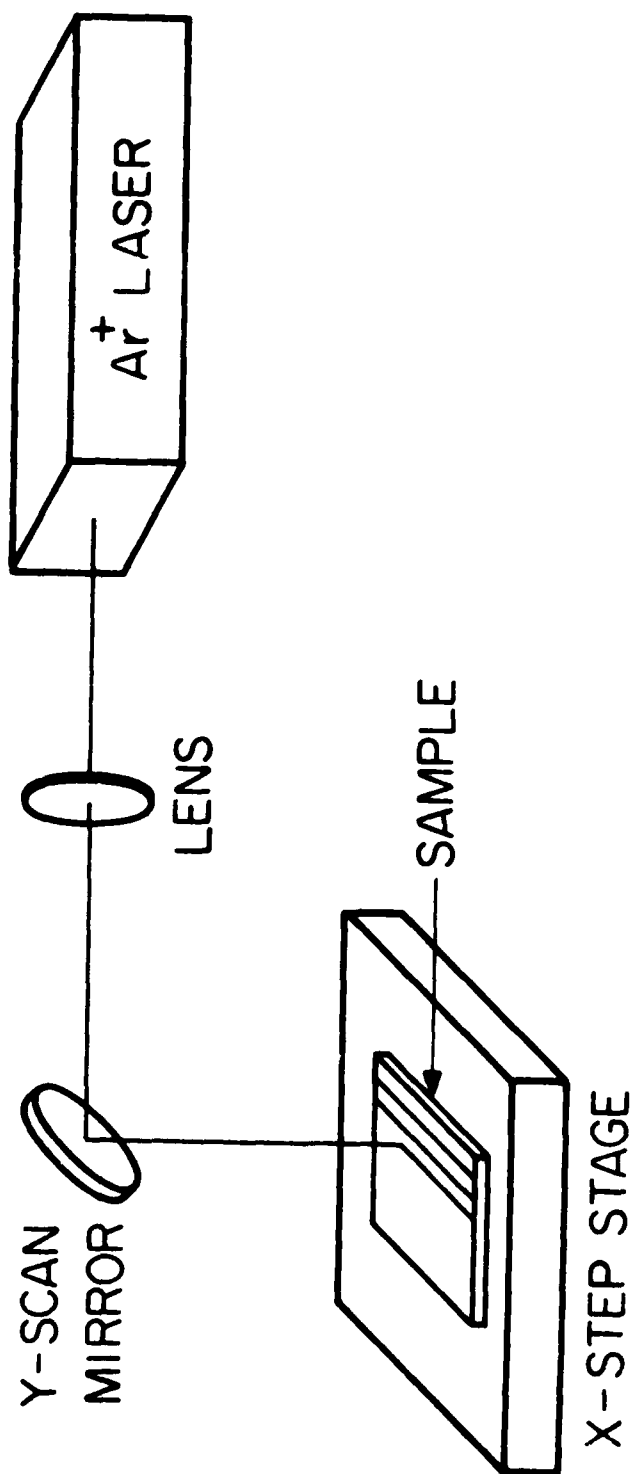
Fig. 12. Low temperature photoluminescence intensity, in normalized units, as a function of annealing laser power for Phosphorus no-phonon line ( $P_{NP}$ ). The intensity of these luminescence lines for thermally-annealed material is indicated by TA. Implant conditions are the same as Fig. 11.  $T_S = 250^\circ\text{C}$ .

Fig. 13. Low temperature photoluminescence intensity, in normalized units, as a function of annealing laser power, for Boron no-phonon line ( $B_{NP}$ ) and TO-phonon line ( $B_{TO}$ ). The intensity of these luminescence lines for thermally-annealed material is indicated by TA. The broken line is the dependence of  $B_{NP}$  on laser power.

for a heavier dose implant, taken from Fig. 5. Implant conditions are the same as Fig. 11.  $T_S = 250^\circ\text{C}$ .

Fig. 14. High resolution spectra of B and P no-phonon luminescence lines for bulk Si conventionally doped with P, and for  $P^{++}$  implanted samples that have been thermally annealed (TA) or laser annealed (LA) at the laser power (normalized to the melting power) indicated. Implant conditions are the same as Fig. 11.  $T_S = 250^\circ\text{C}$ .

# LASER ANNEALING (LA)

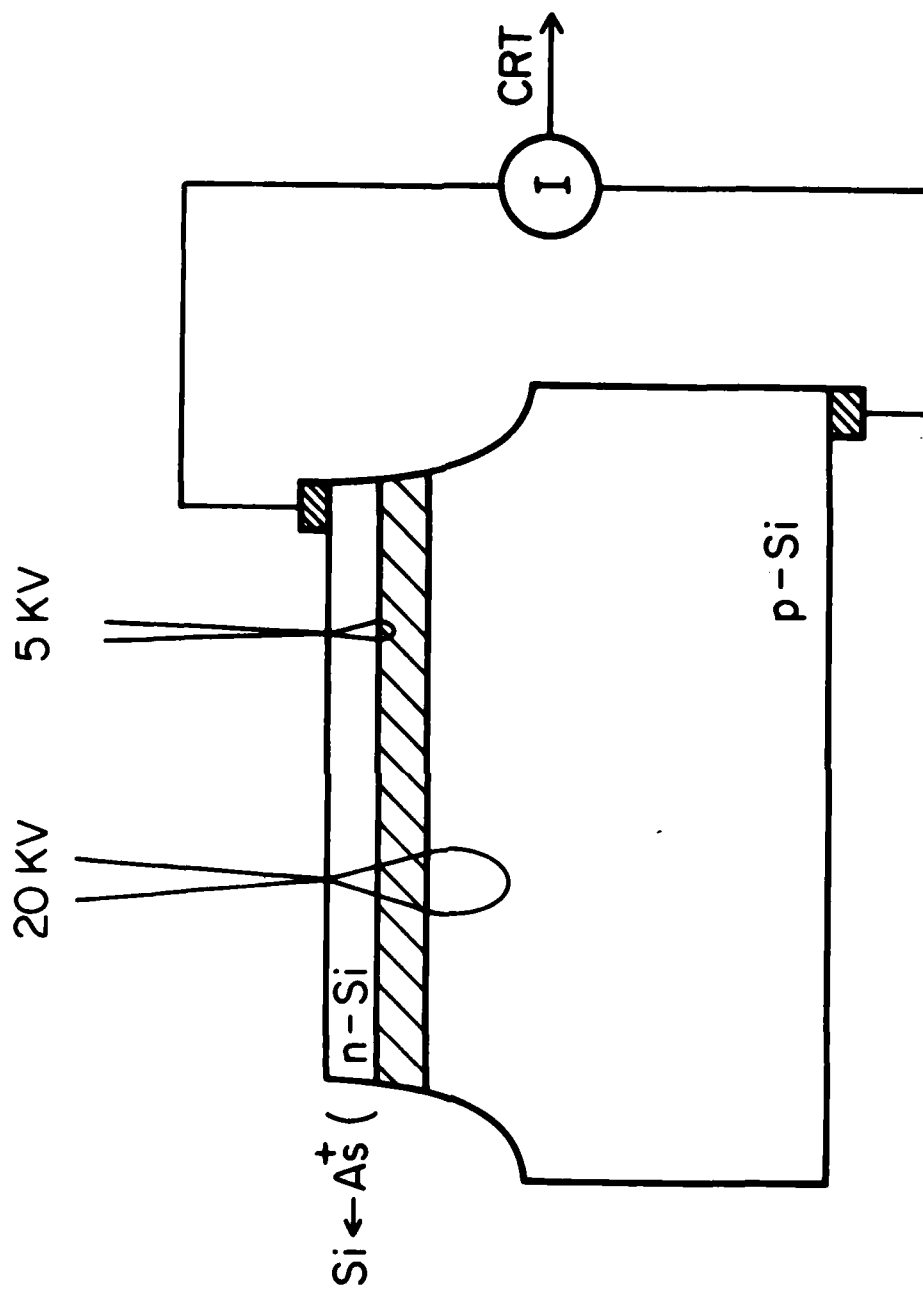


(28)

Fig. 1



# ELECTRON BEAM-INDUCED CURRENT (EBIC)



(29)

Fig. 2

(30)

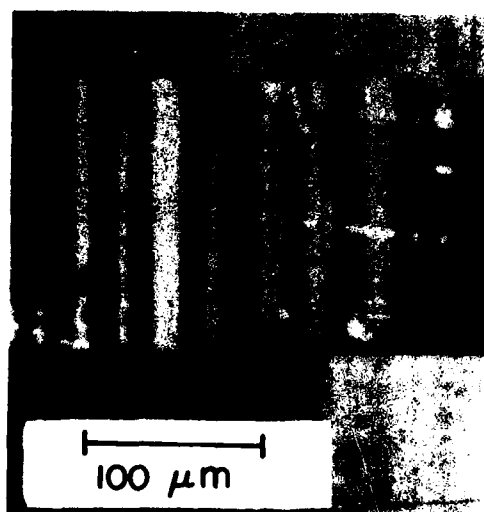


Fig. 3

(31)

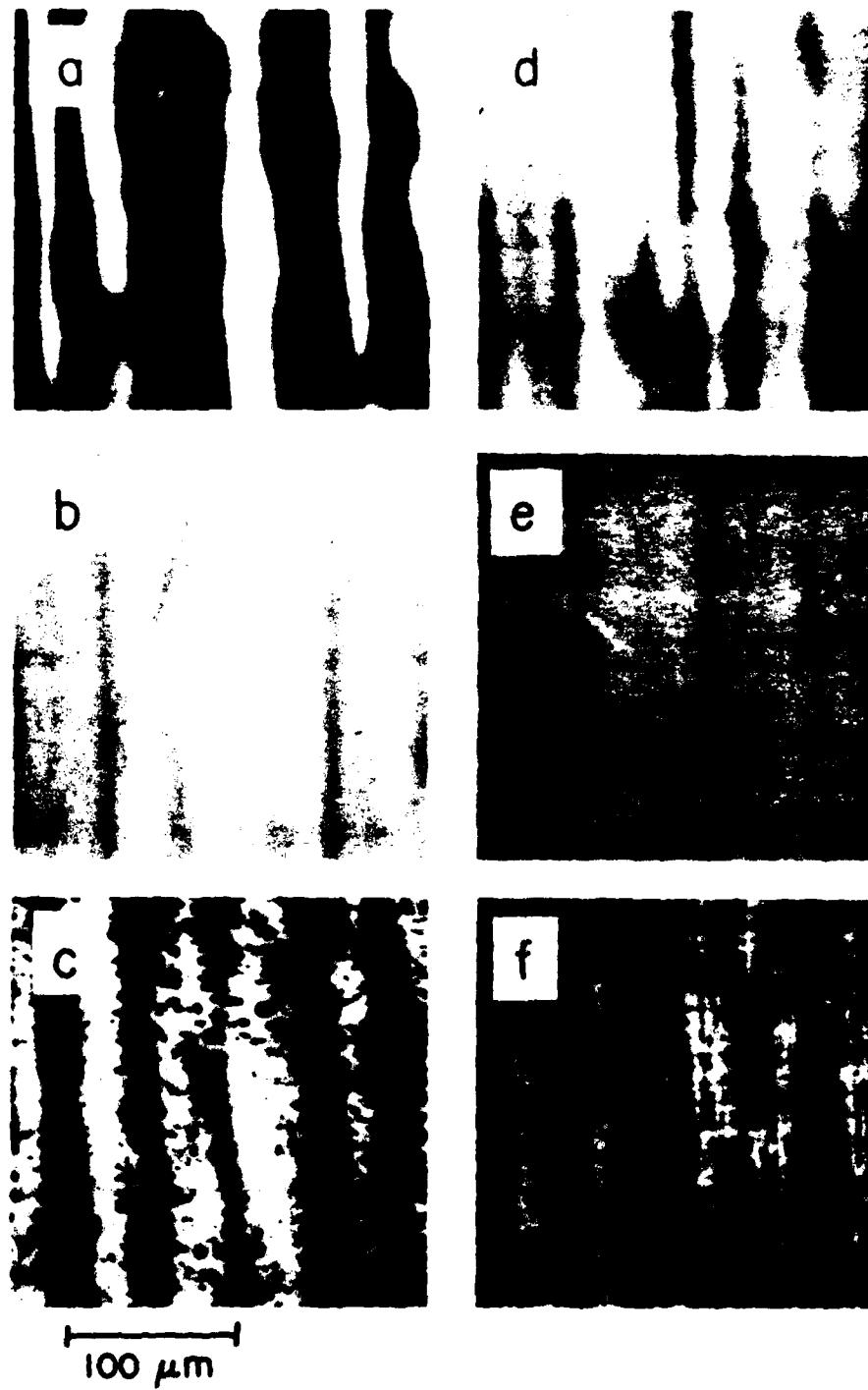


Fig. 4

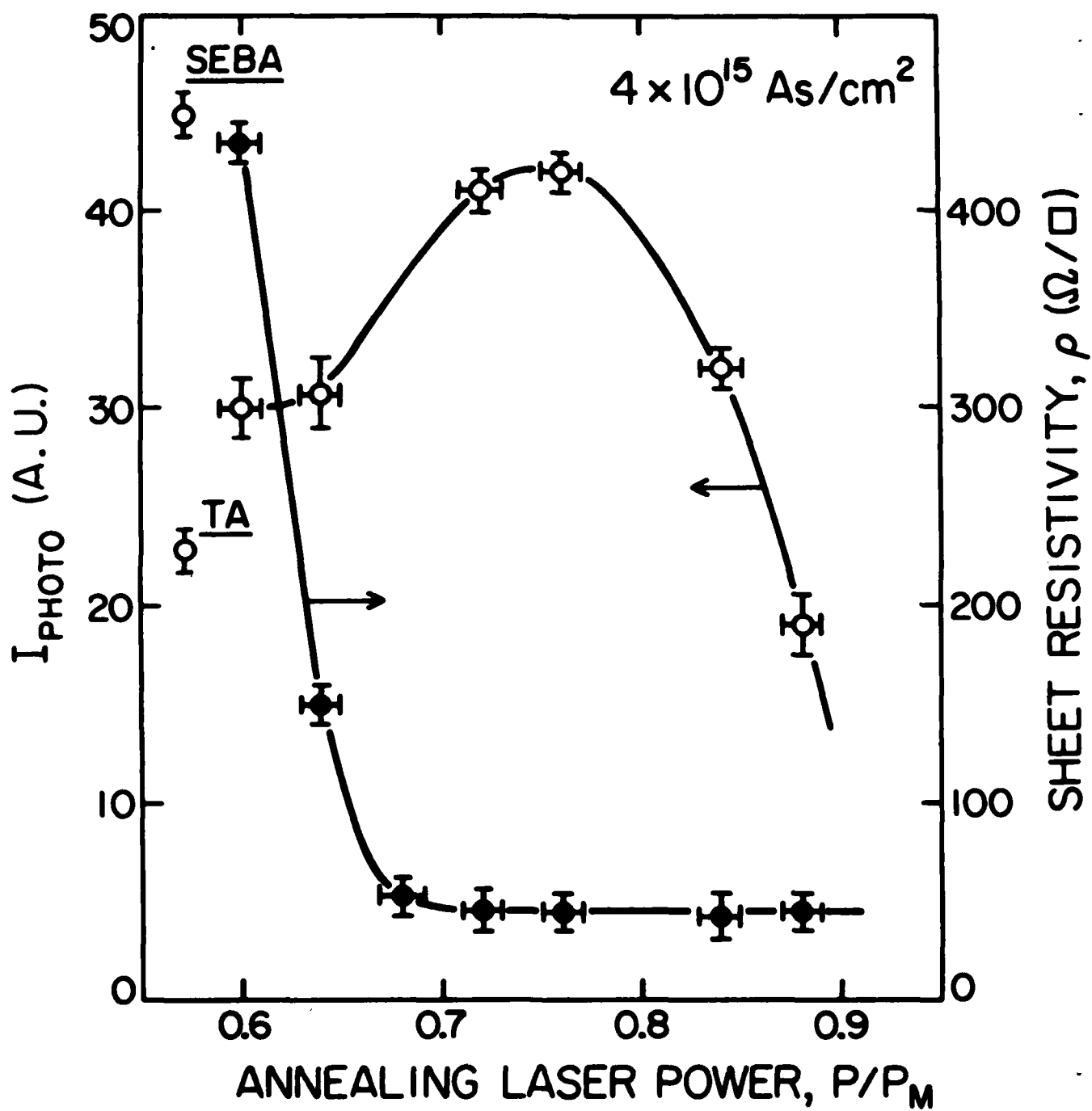


Fig. 5

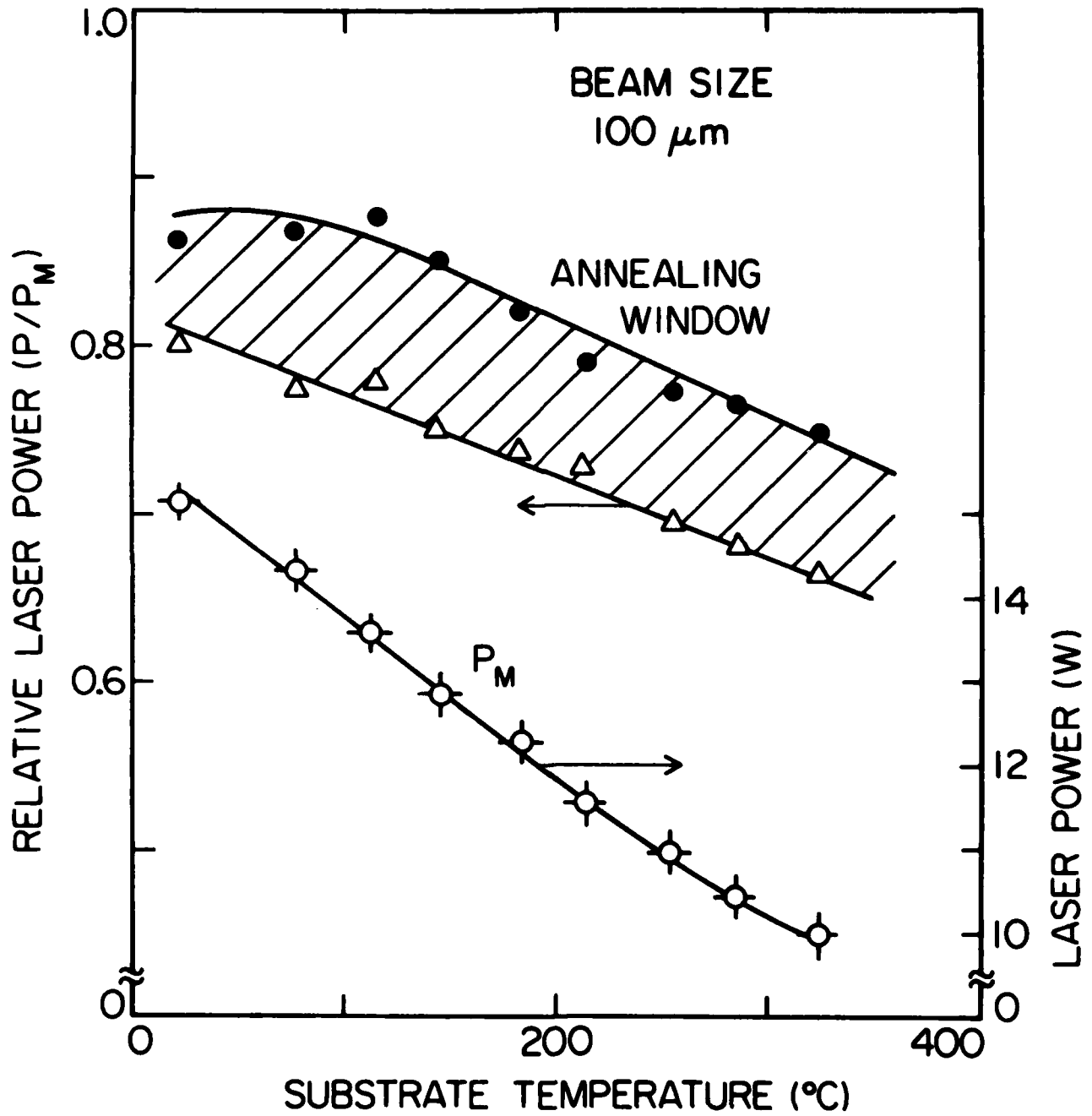
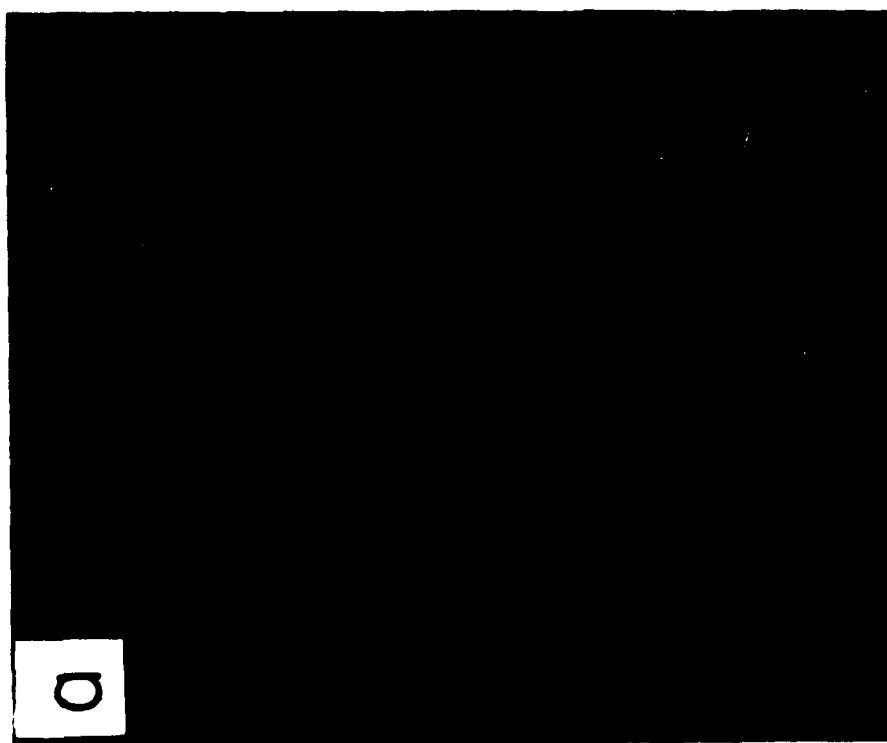
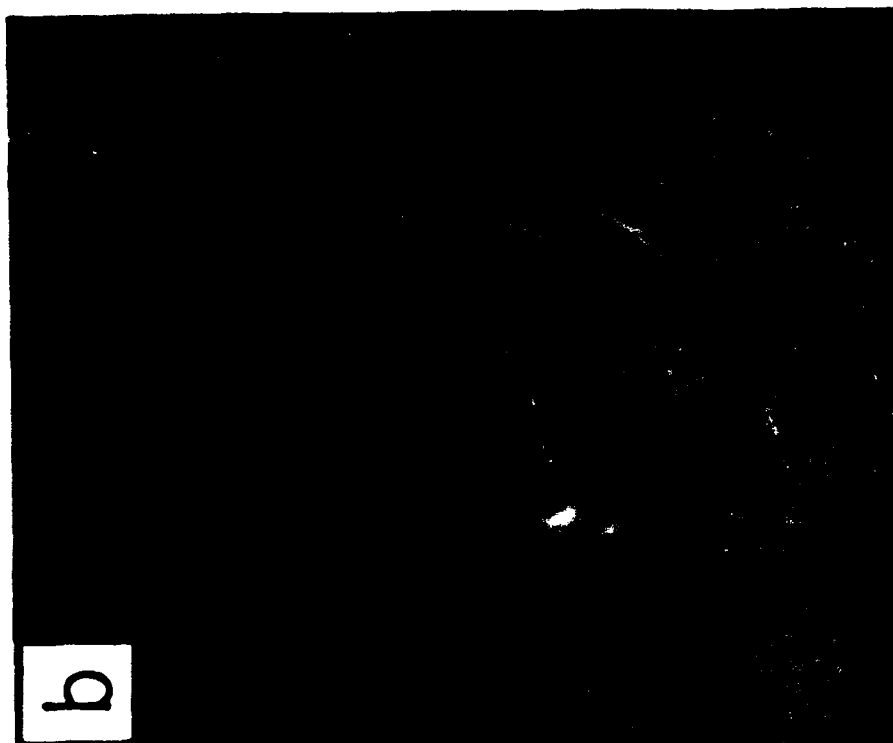


Fig. 6

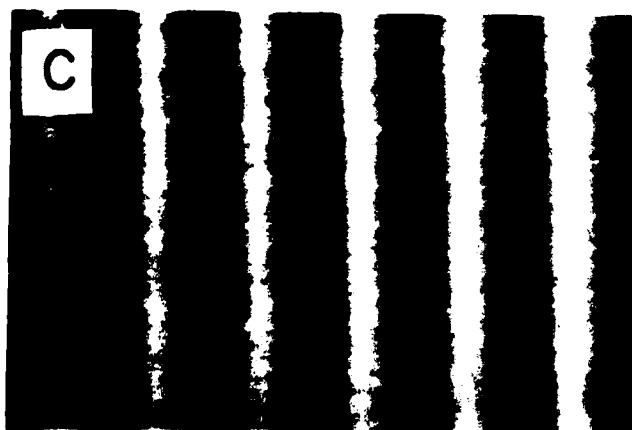
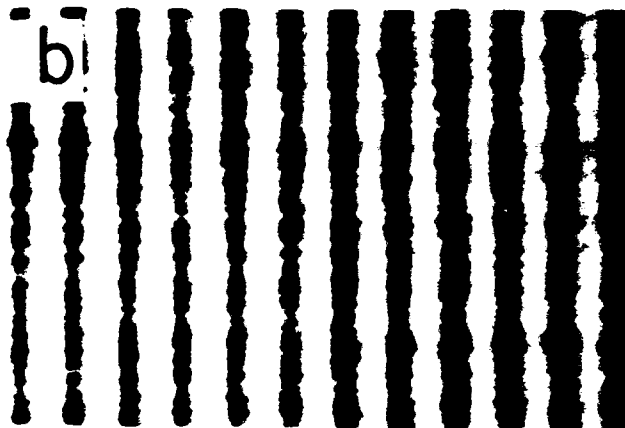
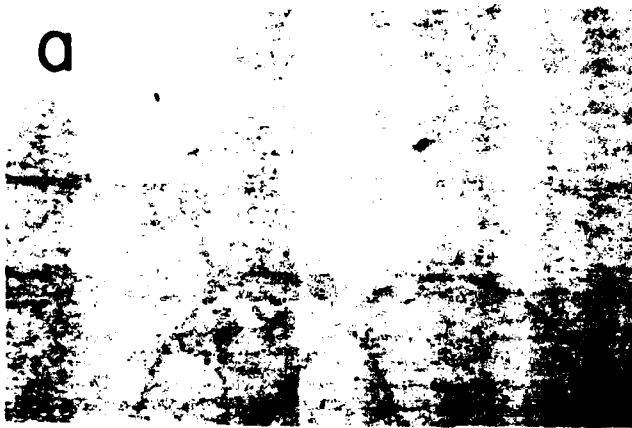
(34)



100  $\mu\text{m}$

Fig. 7

(35)



100  $\mu\text{m}$

Fig. 8

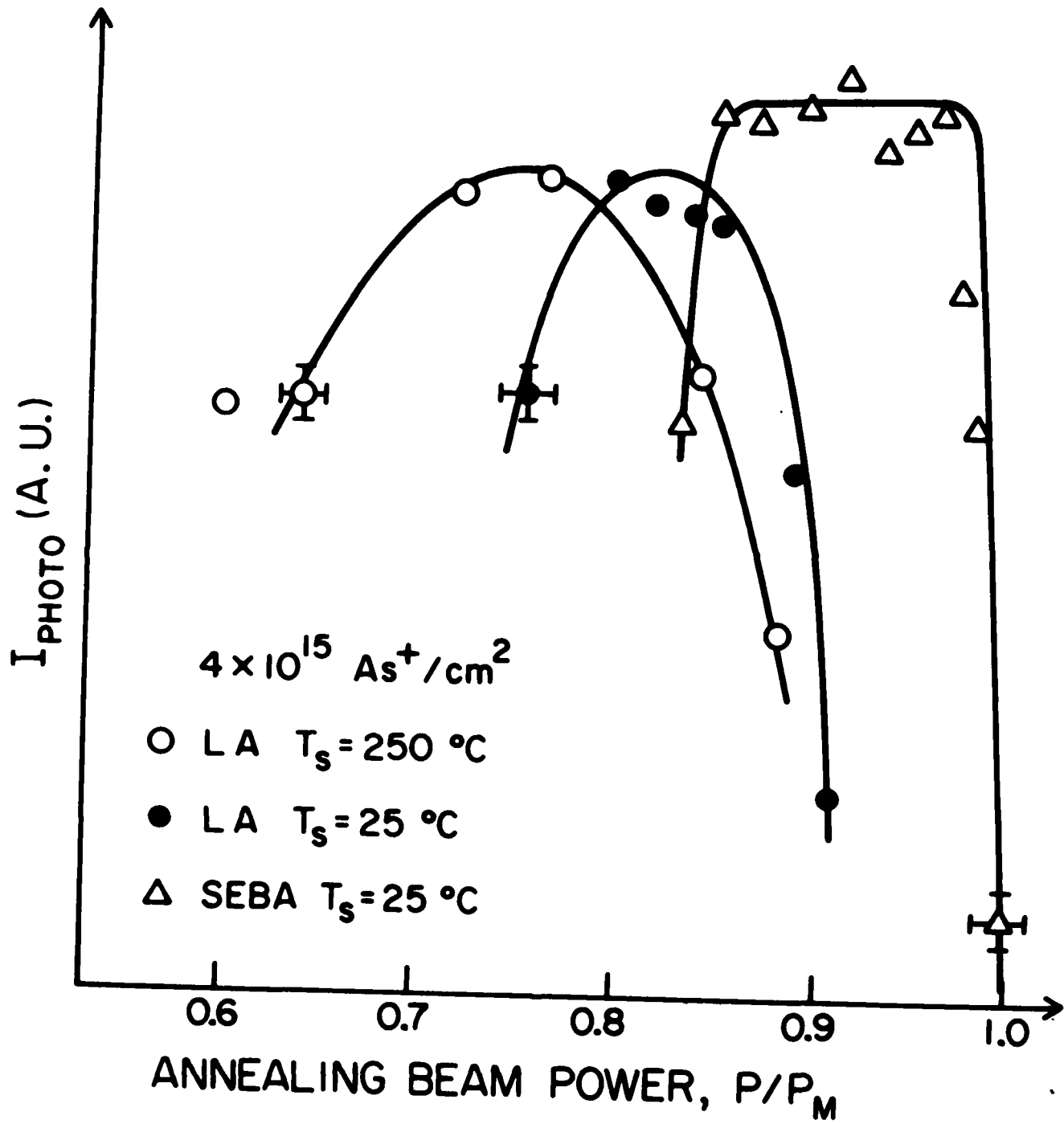
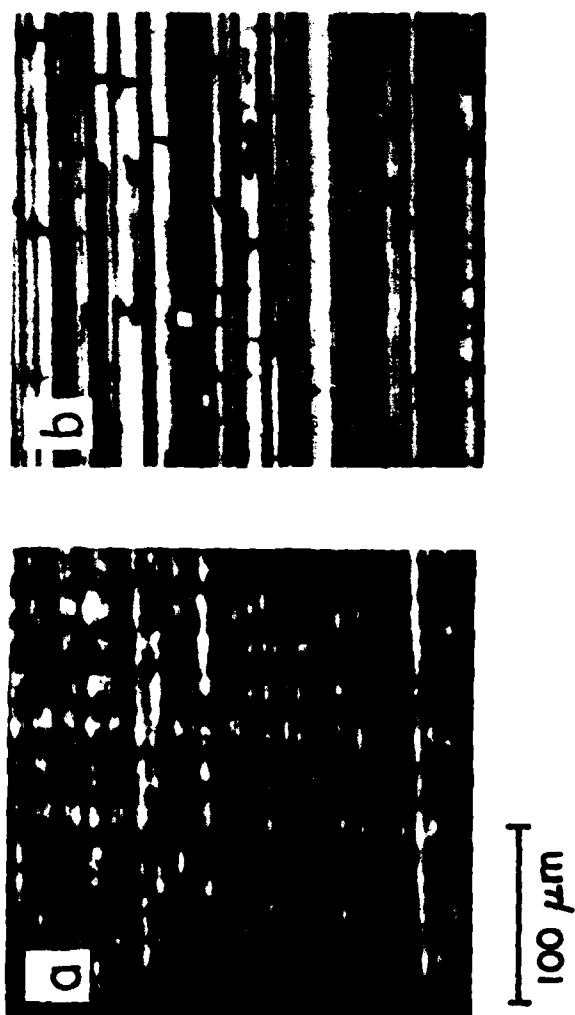


Fig. 9



(37)

Fig. 10



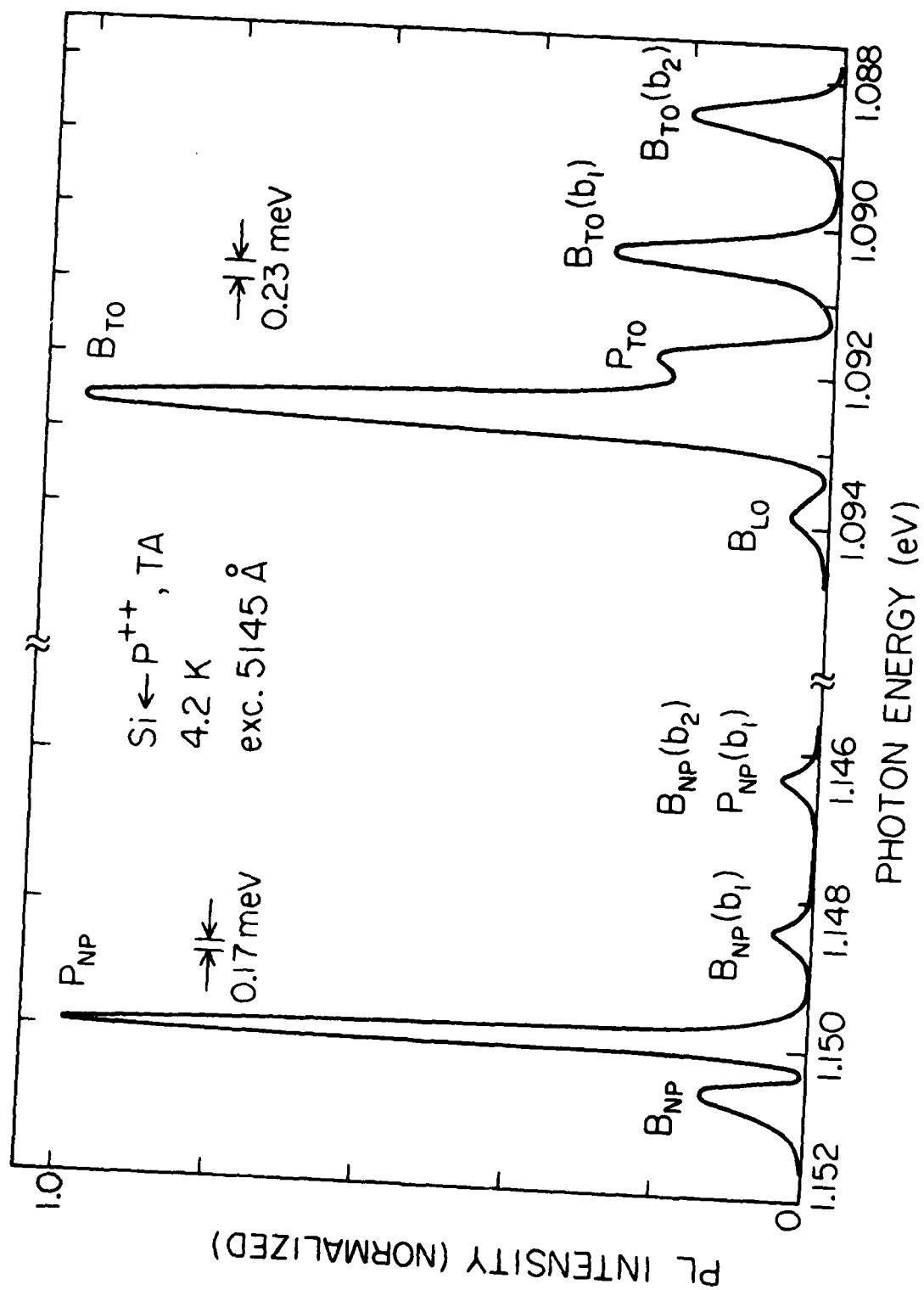


Fig. 11

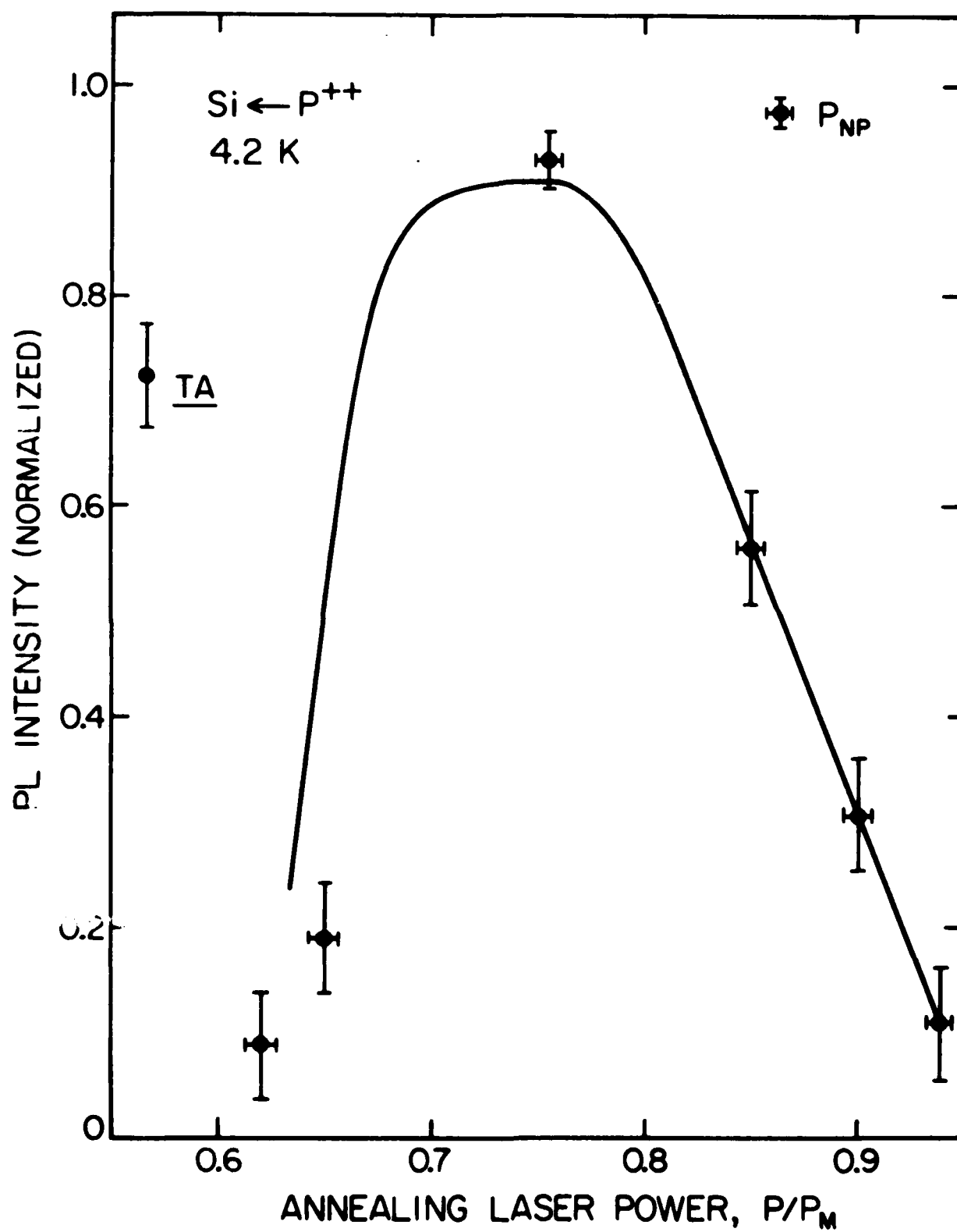
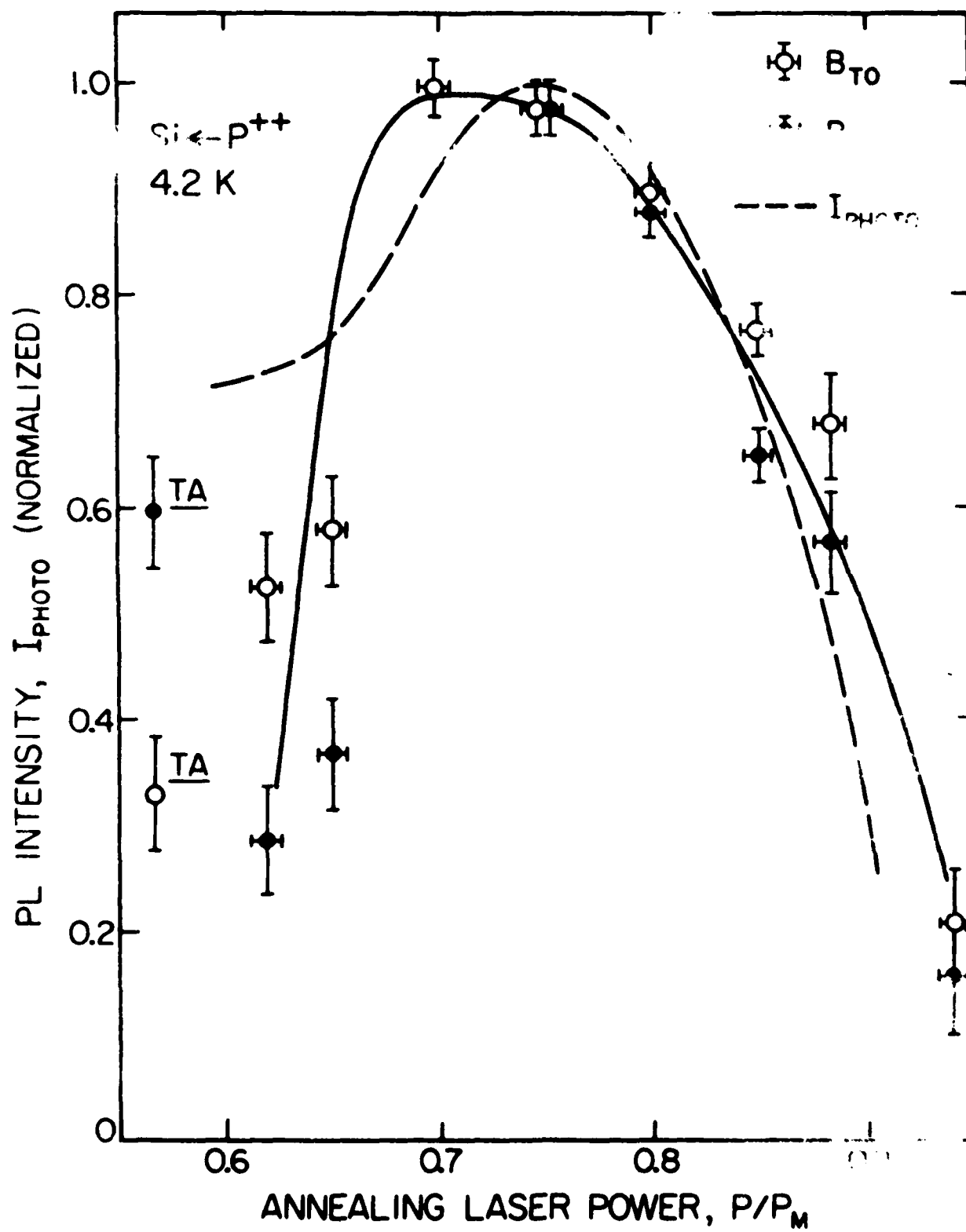


Fig. 12



(41)

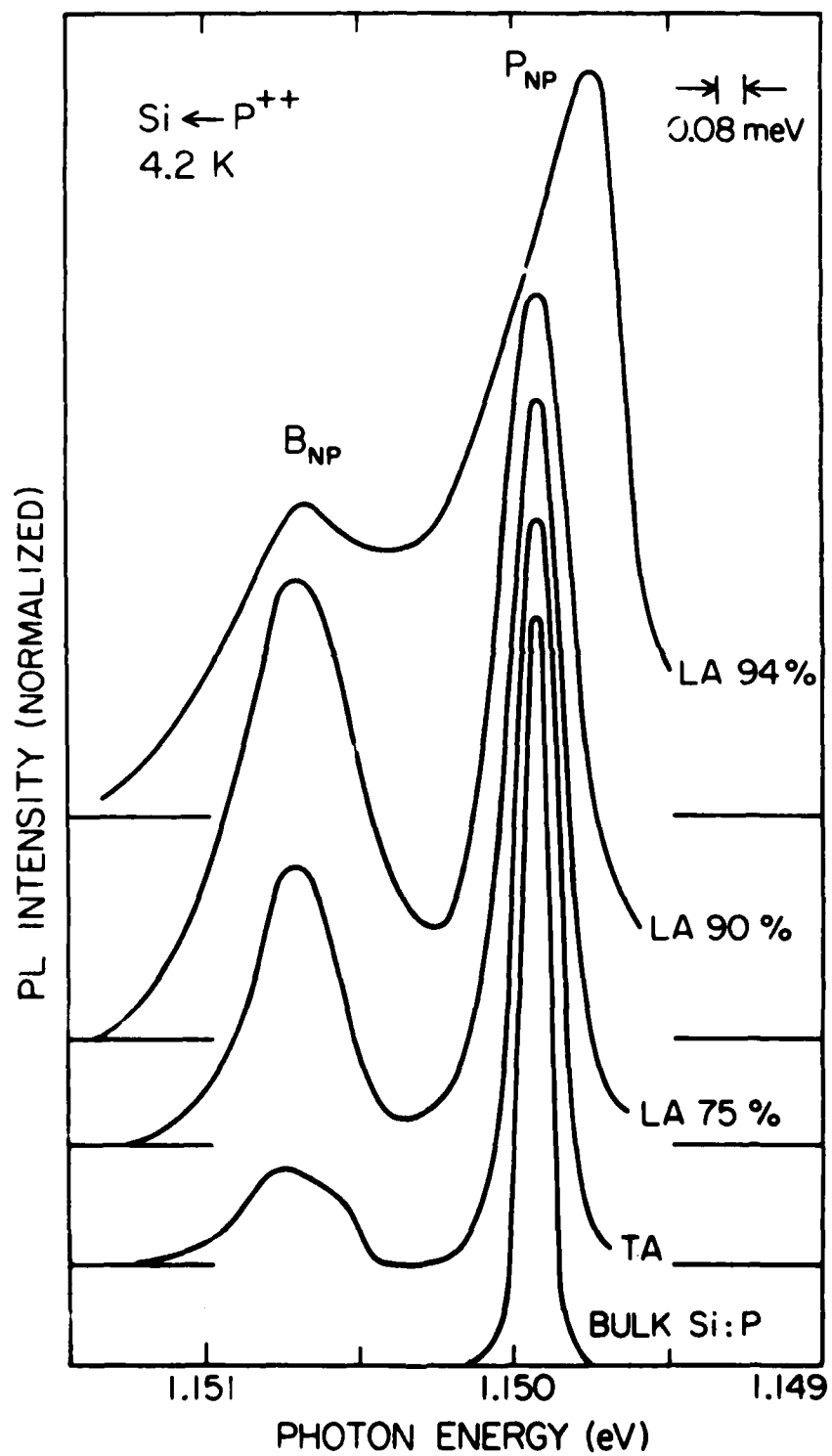


Fig. 14



DATE  
ILME  
—8